LETTER

Measurement of a helical Pfirsch–Schlüter current with reduced magnitude in HSX

J.C. Schmitt[a], J.N. Talmadge and D.T. Anderson

Department of Electrical and Computer Engineering, University of Wisconsin-Madison, Madison, Wisconsin 53706, USA

E-mail: jschmitt@pppl.gov

Abstract

Measurements of the helical rotation and the reduction of the magnitude of the Pfirsch–Schlüter current compared to an equivalent tokamak are reported in a device that has quasihelical symmetry. The Pfirsch–Schlüter current is helical due to the lack of toroidal curvature, and is reduced in magnitude by the high effective transform. A 3D equilibrium reconstruction based on magnetic diagnostics agrees well with the profiles measured with Thomson scattering and diamagnetic flux loop measurements.

(Some figures may appear in colour only in the online journal)

Optimized stellarators as fusion reactors offer the possibility of excellent confinement of alpha particles while minimizing the problems associated with disruptions, current drive and positional stability. The concept of the quasihelical stellarator (QHS) was first discovered numerically by Nührenberg and Zille in 1988 [1]. Recent calculations have shown the possibility of achieving high beta, $\beta = 2\mu_0 \langle p/B^2 \rangle$ (where the brackets denote the flux surface average), in a QHS device [2]. Such a device has a single dominant helical component in the magnetic field spectrum so that $|B|$ is almost constant along a helical ribbon on a flux surface. There is little to no toroidal curvature component in the magnetic field spectrum.

The helically symmetric experiment (HSX) is the experimental realization of the QHS concept [3]. Reduced flow damping [4] and improved neoclassical transport [5] in HSX have been reported. One unique aspect of a QHS machine is that it has a high effective transform given by $t_{\rm eff} = n - mt$, where n and m are the toroidal and poloidal mode numbers of the main spectral component of the magnetic field and t is the rotational transform. For HSX where $n = 4$, $m = 1$ and $t = 1/q$ is 1.05 at the axis and 1.12 at the edge, the effective transform is about 3. Compared to the physical transform, the high effective transform in HSX results in reduced drift of passing particles from a magnetic surface. This was experimentally verified with an electron gun, fluorescent mesh and a camera [6]. As a result of the high effective transform, the Pfirsch–Schlüter current is correspondingly small, as is the

resultant shift of the plasma axis, the Shafranov shift. In other stellarators and tokamaks the toroidal curvature drives a dipole current which varies little with toroidal angle. In HSX, the helical curvature drives a current that rotates helically along the torus. Previously, the dipole field due to this current was measured in the Heliotron E device, an unoptimized stellarator [7]. Also, a reduced Shafranov shift due to optimization was measured in W7-AS [8] using flux loops and soft x-ray tomography. In this letter, we present the first demonstration that the Pfirsch–Schlüter current in a QHS rotates helically and is reduced in magnitude compared to a tokamak because of the high effective transform. The results serve to confirm the lack of toroidal curvature in HSX. Furthermore, these results were obtained using the V3FIT [9, 10] code that allows for the 3D equilibrium reconstruction of the plasma pressure and current profiles.

In the absence of an ohmic current or current drive, the parallel current consists of the Pfirsch–Schlüter current (which integrates to zero on a flux surface) and the bootstrap current. By employing Boozer flux coordinates [11] where ζ and θ are the toroidal and poloidal angular coordinates, respectively, the Pfirsch–Schlüter current can be written as [12]

$$J_{\rm PS} = \frac{B}{B_0^2} \frac{{\rm d}p}{{\rm d}\Phi} \sum_{(n,m)^*} \frac{nI + mF}{n - mt} \delta_{n,m} \cos\left(n\zeta - m\theta\right). \quad (1)$$

The quantities Φ and I are, respectively, the toroidal flux and toroidal current enclosed within a flux surface and F is the total poloidal current external to a flux surface. The $\delta_{n,m}$ terms are the coefficients of the Fourier expansion of
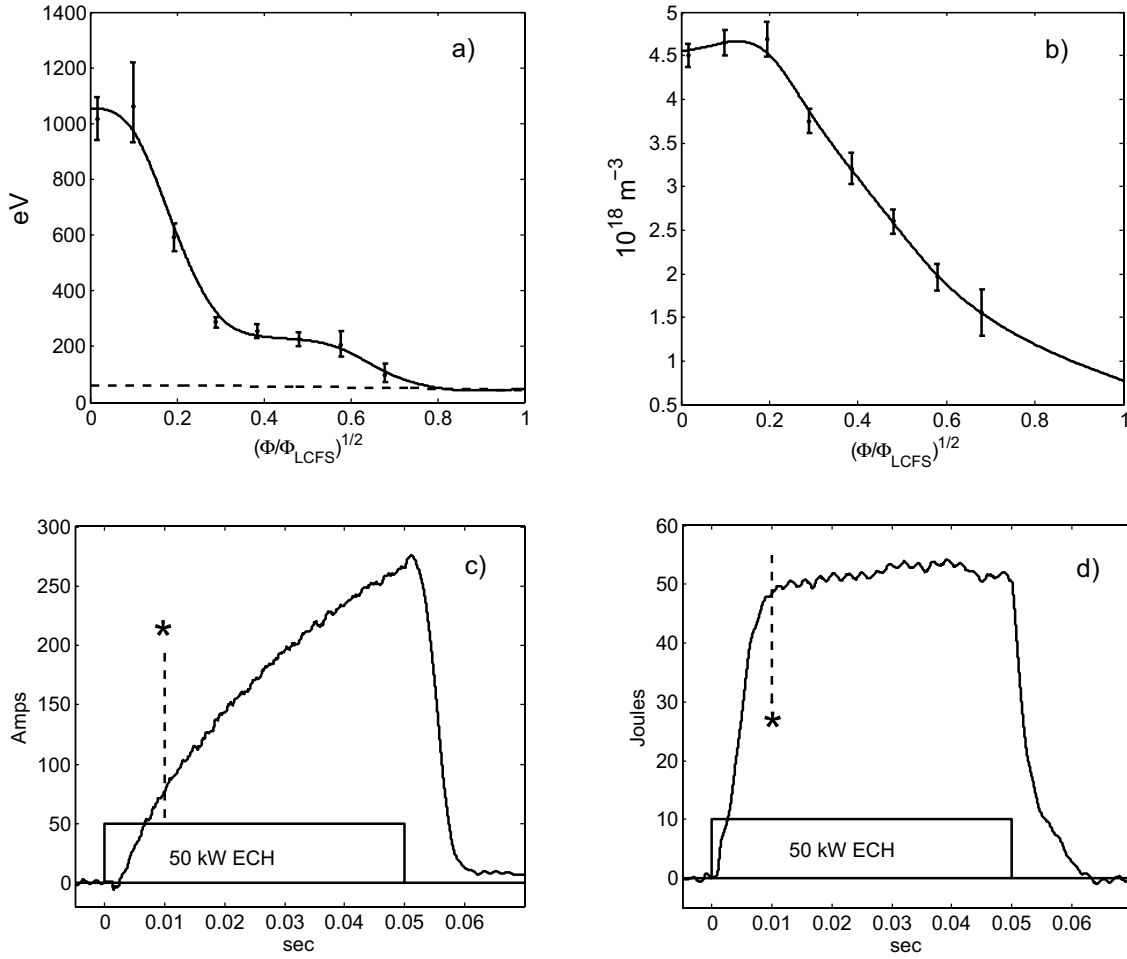
Figure 1. (*a*) Temperature profiles of electron (solid) and ions (dashed), (*b*) electron density profile, (*c*) time evolution of the total integrated current, (*d*) time evolution of the measured stored energy (from the diamagnetic loop). *Dashed lines indicate the time for which the reconstruction is performed.

$1/B^2$ along a field line. The summation over the magnetic field spectral components excludes the $(n, m) = (0, 0)$ term. For HSX, in which the current driven by the toroidal curvature $\delta_{0,1}$ is vanishingly small, the Pfirsch–Schlüter current is overwhelmingly dominated by the principal spectral component, $\delta_{4,1}$. There are three unique features of the current in a QHS configuration: first, the dipole current rotates with the helical $|B|$ contours due to the $\cos(4\zeta - \theta)$ dependence. Second, in the region $\zeta = 0$ where the $|B|$ contours are similar to that in a tokamak (i.e. low magnetic field on the outboard side of the device), the dipole current has the opposite polarity compared to a tokamak. This is because the $B \times \nabla B$ drift is in the opposite direction compared to a tokamak [6]. Third, the magnitude of the current in a QHS device is reduced by the factor $n - m\iota$, the effective transform. This factor can be much larger than the corresponding term for a tokamak, which is just the transform, because the major spectral component is $(n, m) = (0, 1)$. This also assumes that the toroidal fields are similar for a QHS device and a tokamak (F is similar), that nI is small (because $n = 0$ in a tokamak and I is small in a stellarator), and that the tokamak $\delta_{0,1} \sim \delta_{4,1}$ component in HSX.

Plasmas in HSX reported here are created and heated in a magnetic field of 1 T by 50 kW of 1st-harmonic O-mode

electron cyclotron resonance heating (ECRH) with a 28 GHz gyrotron. The launch angle is perpendicular to the magnetic axis: no current drive associated with the ECRH has been observed [13]. The plasmas are fueled with hydrogen gas injected with a piezoelectric gas valve located on the opposite side of the torus from the ECRH. Electron temperature and density profiles, figure 1, are measured with a Thomson scattering system. Doppler spectroscopy measurements indicate ion temperatures in the range 40–65 eV. Estimates for the effective ion charge during typical operations give $Z_{\text{eff}} \approx 1$–3 across much of the plasma column, rising to higher levels near the edge.

The magnetic diagnostic set consists of a Rogowski coil, a diamagnetic loop and three sets of coils located at three separate toroidal locations as shown in figure 2. Two of the sets are external to the vacuum chamber and are separated by 1/3 of a field period. The external sets each have 16 coils spaced poloidally about the plasma that measure changes in the local magnetic field vector in their own local orthogonal coordinate system. The radial component of the magnetic field (B_r) points in a direction that is inward normal to the vacuum vessel and the poloidal component (B_θ) is tangent to the vessel in a nearly constant ζ (toroidal) plane. These two sets of coils measure the helical structure of the plasma. A third set of coils
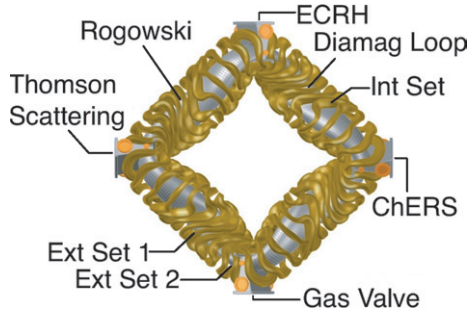
Figure 2. Top view of the HSX stellarator (vacuum vessel and field coils) along with the toroidal locations of the diamagnetic loop, Rogowski coil and the three sets of magnetic diagnostics indicated. The locations of the ECRH, gas valve, Thomson scattering and charge exchange recombination spectroscopy (ChERS, for ion Doppler spectroscopy measurements) are also shown.

that is interior to the vacuum vessel consists of 15 coils that only measure the poloidal component of the magnetic field. This third set is used to measure the absolute magnitude of the magnetic field. The diamagnetic loop is a 10-turn loop installed inside of the vacuum vessel and measures changes to the enclosed toroidal flux at a nearly constant ζ plane.

Figure 1(*c*) shows the time evolution of the total integrated current which does not reach steady state by the end of the 50 ms discharge. The effective L/R time constant in HSX varies from 20 to 60 ms depending on the plasma temperature and conductivity. A steady-state current is only reached during the 50 ms of the gyrotron pulse in discharges where the resonance is off-axis and the core temperature drops to 400 eV. In contrast to the L/R time, the stored energy of the plasma measured by the diamagnetic loop reaches steady state about 10 ms after the initiation of the discharge as shown in figure 1(*d*). The stored energy from the diamagnetic loop is 50 J, compared to the integrated kinetic stored energy of 52 J from the Thomson scattering and spectroscopy measurements. The volume-averaged beta is under 0.04% and has a negligible effect on the vacuum equilibrium. The analysis of the Pfirsch–Schlüter current is performed at 10 ms, before the bootstrap current has reached substantial levels and dominates the plasma contribution of the measured magnetic field.

Using the pressure profile calculated from the measured profiles of figure 1 and assuming $Z_{eff} = 1$, the three-dimensional equilibrium code VMEC [14] is used to calculate the Pfirsch–Schlüter current. This is shown in figure 3 along with the approximate locations of the three coil sets. The region of ($J_{PS} < 0$) rotates from the inboard side of the plasma column at the $\approx 1/2$ field period location to the outboard side at $\approx 1/6$ field period location. A sketch of the magnetic field generated by this current distribution is also shown in the figure. The code V3FIT was used in the forward direction (that is without equilibrium reconstruction) to calculate the poloidal and radial components of the local magnetic field at poloidal indices 1–32 (defined in figure 3) due to only the Pfirsch–Schlüter current. This is shown in figure 4 by the dashed curves. The characteristics of the dipole magnetic field are seen in the calculated signals. The radial component of the signals is largest near indices 4, 12, 24 and 32, and the sign of the signals is consistent with the rotation of the current. The zero crossings of the poloidal components of the magnetic field

are at those same indices. The sign of the poloidal signals is positive for indices 5–11 and 17–23, and negative for indices 13–16 and 25–31.

As seen in figure 1(*c*), there is a net current of about 80 A flowing in the plasma when the measurements shown in figure 4 were made at $t = 10$ ms, indicating that the Pfirsch–Schlüter current is not the only current that needs to be considered when comparing to the measurements. A steady-state calculation of the bootstrap current was obtained with a neoclassical transport code, PENTA [15, 16], which includes momentum conservation between the plasma species [17]. The net current that flows at a given time is the sum of the steady-state bootstrap current and the current that flows because of the induced electric field. The decay of this induced electric field is calculated with a model that includes the 3D nature of the plasma column [18, 19]. The magnetic signals at the diagnostic coils due to the sum of the contributions from the Pfirsch–Schlüter and bootstrap current were calculated by V3FIT and shown in figure 4 by the solid curves. The measurements from the diagnostic coils are shown in the figure by the vertical lines which indicate the errors in the measurements. The effect of the bootstrap current on the diagnostic signals is to add an offset to the poloidal field measurements while the modifications to the radial field are more subtle. In terms of sign and phase, there is good agreement between the measured and modelled diagnostic signals. In particular, the rotation of the B_θ components between the 1/6 field period and 1/2 field period locations clearly demonstrates the rotation of the Pfirsch–Schlüter current. The disagreement between the simulation and measurement of B_θ for indices 1–4, 12–16, 25–32 and of B_r for indices 3–7, 10–12, 17–19, 24–25 is likely due to eddy currents in the vacuum vessel which have not been modelled at this point.

Because of the possibility of eddy currents being induced in the vacuum chamber, we use the set of coils internal to the vacuum chamber to determine whether the absolute magnitude of the Pfirsch–Schlüter current is reduced by the high effective transform in HSX. Here we use V3FIT in the backward direction to perform a 3D equilibrium reconstruction. The measured and calculated signals for the internal diagnostics, indices 33–47, are shown in figure 5. During the reconstruction, V3FIT minimizes the mismatch between the measured (observed) and modelled signals, S_o and S_m, weighted by the uncertainty of the signal for each diagnostic, σ:

$$\chi^2(\boldsymbol{p}) = \sum_i \left(\frac{S_{o,i} - S_{m,i}(\boldsymbol{p})}{\sigma_i} \right)^2. \qquad (2)$$

The subscript i indicates a particular diagnostic. The set of parameters used to describe the plasma profiles is designated as the parameter vector, $\boldsymbol{p}$.

The pressure profile, as a function of a radial coordinate, $s = \Phi/\Phi_{LCFS}$ (Φ_{LCFS} is the toroidal flux through the last closed flux surface), is modelled by a Lorentz-type expression with two parameters (P_0, AM):

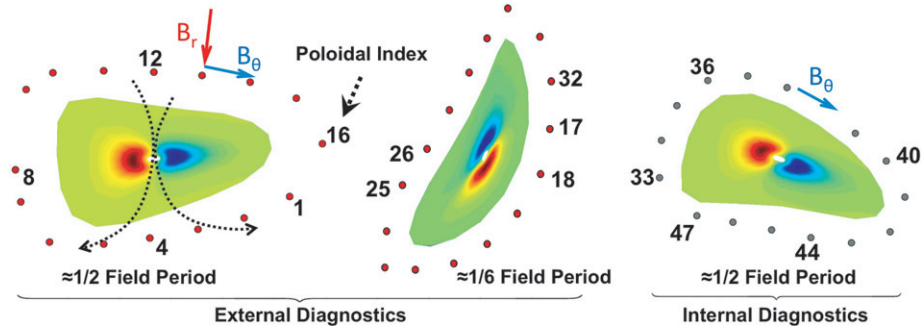$$\frac{p(s)}{P_0} = 2 \left(1 + s^{AM} \right)^{-1} - 1. \qquad (3)$$

Figure 3. The Pfirsch–Schlüter current density and location of magnetic diagnostics at three toroidal locations corresponding to Ext Set 1, Ext Set 2 and Int Set in figure 2. The red contours indicate current directed into the plane ($J_{PS} < 0$) while blue contours indicate current out of the plane ($J_{PS} > 0$). The dipole magnetic field generated by this current density is indicated by black arrows on the left plot.
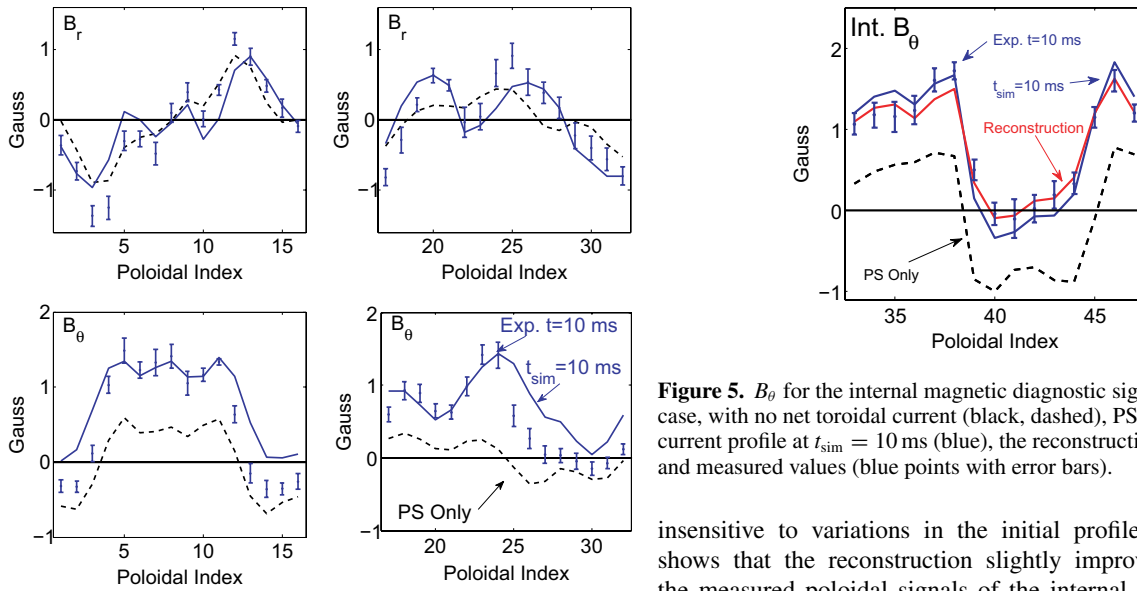

Figure 4. B_r and B_θ components of the external magnetic diagnostic signals: Pfirsch–Schlüter only case, with no net toroidal current (black, dashed), PS current plus evolved current profile at $t_{sim} = 10$ ms (blue) and measured values (blue points with error bars).

The enclosed current profile is modelled by an arctangent function with two parameters (I_{tor}, AC):

$$I_{enclosed}(s) \propto \arctan\left(\frac{ACs^{3/2}}{1-s}\right). \quad (4)$$

The normalization is determined by the total enclosed toroidal current:

$$I_{enclosed}(s = 1) = I_{tor}. \quad (5)$$

The initial guess for the plasma pressure profile was a best fit to the measured profile, and the initial guess of the current profile was a best fit to the calculated bootstrap current at $t = 10$ ms. During the reconstruction, V3FIT was allowed to adjust P_0, AM, I_{tor}, AC, and the net toroidal flux enclosed within the last closed flux surface.

Figure 6 shows the measured and reconstructed pressure profiles and calculated and reconstructed current profiles. During the process χ^2 reduces from 29.8 to 9.6. The final reconstructed profiles with the lowest χ^2 were found to be

Figure 5. B_θ for the internal magnetic diagnostic signals: PS only case, with no net toroidal current (black, dashed), PS + evolved current profile at $t_{sim} = 10$ ms (blue), the reconstruction best fit (red) and measured values (blue points with error bars).

insensitive to variations in the initial profiles. Figure 5 shows that the reconstruction slightly improves the fit to the measured poloidal signals of the internal coil set. The reconstructed pressure profile in particular agrees well with the measured profile. To test the sensitivity of the reconstructed profiles, the pressure profile was varied by adjusting the pressure parameters (i.e. P_0 and AM) while holding the current parameters at their reconstructed values, and then searching for profiles which fell within a 1-σ deviation of the minimum χ^2. This showed that the pressure profile was robust except near the magnetic axis. The process was then repeated for the current profile, while keeping the pressure parameters at their reconstructed values. For this case, it was found that the most important parameter was the total current enclosed inside $s = 1$, which allowed matching the DC shift to the poloidal field as shown in figure 5. With only one internal diagnostic set, the constraints on the current profile reconstruction were not sufficient to limit the range of current profiles that integrate to the same total enclosed current. Representative error bars for the reconstructed profiles are shown in red in figure 6.

For VMEC, specification of the input pressure profile determines the Pfirsch–Schlüter current whereas the bootstrap current is specified by an input current profile. The measurements shown here were purposefully made early in the discharge so that the bootstrap current would be small. From figure 4 it can be seen that the magnetic diagnostics are very sensitive to the Pfirsch–Schlüter current and not so much to the bootstrap current which basically adds a dc shift to the poloidal
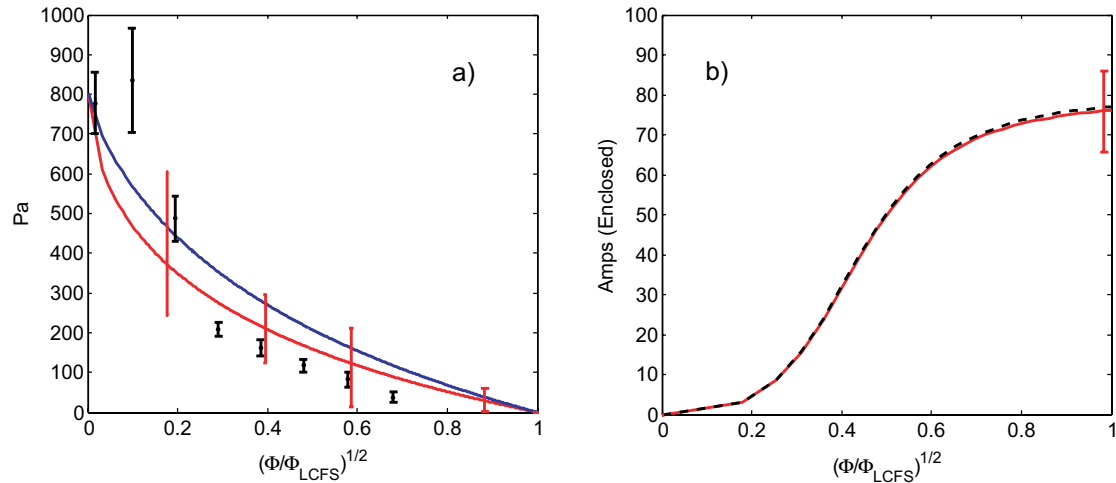
Figure 6. (*a*) Measured (black), best fit to the measured data points and initial guess (blue) and reconstructed (red) plasma pressure and (*b*) initial guess (black dashed lines) and reconstructed (red) enclosed plasma current profile. Representative error bars for the reconstructed profiles are shown in red.

field signals. Hence, because the reconstructed pressure profile agrees with the measurements, this confirms the reduction of the Pfirsch–Schlüter current in a QHS device because of the high effective transform and the lack of toroidal curvature.

In a tokamak with the identical transform, magnetic field strength and pressure gradient as in HSX, the Pfirsch–Schlüter current would be about 3 times larger. Because of the reduced Pfirsch–Schlüter current in HSX, the shift of the magnetic axis is reduced compared to a similar tokamak, a property of QHS configurations as originally discussed by Nührenberg and Zille [1].

Acknowledgments

References

[1] Nührenberg J. and Zille R. 1988 *Phys. Lett.* A **129** 113
[2] Ku L.P. and Boozer A.H. 2011 *Nucl. Fusion* **51** 013004
[3] Anderson F.S.B., Almagri A.F., Anderson D.T., Mathews P.G., Talmadge J.N. and Shohet J.L. 1995 *Fusion Technol.* **27** 273 http://scitation.aip.org/getabs/insref_abs.jsp?key=PHPAEN&prog=getinsref&id=5060553&idtype=inspec
[4] Gerhardt S.P., Talmadge J.N., Canik J.M. and Anderson D.T. 2005 *Phys. Rev. Lett.* **94** 015002
[5] Canik J.M., Anderson D.T., Anderson F.S.B., Likin K.M., Talmadge J.M. and Zhai K. 2007 *Phys. Rev. Lett.* **98** 085002
[6] Talmadge J.N., Sakaguchi V., Anderson F.S.B. and Almagri A.F. 2001 *Phys. Plasmas* **8** 5165
[7] Besshou S., Fujita N., Ogata K., Kondo K., Kurimoto Y., Mizuuchi T., Nagasaki K., Okada H., Sano F. and Obiki T. 1997 *Nucl. Fusion* **37** 13
[8] Hirsch M. *et al* 2008 *Plasma Phys. Control. Fusion* **50** 053001
[9] Hirshman S.P., Lazarus A., Hanson J.D., Knowlton S.F. and Lao L.L. 2004 *Phys. Plasmas* **11** 595
[10] Hanson J.D., Hirshman S.P., Knowlton S.F., Lao L.L., Lazarus E.A. and Shields J.M. 2009 *Nucl. Fusion* **49** 075031
[11] Boozer A.H. 1982 *Phys. Fluids* **25** 520
[12] Boozer A.H. 1981 *Phys. Fluids* **24** 1999
[13] Schmitt J.C., Talmadge J.N. and Lore J. 2010 *Control. Plasma Phys.* **50** 745
[14] Hirshman S.P. and Whitson J.C. 1983 *Phys. Fluids* **26** 3553
[15] Spong D.A. 2005 *Phys. Plasmas* **12** 056115
[16] Lore J., Guttenfelder W., Briesemeister A., Anderson D.T., Anderson F.S.B., Deng C.B., Likin K.M., Spong D.A., Talmadge J.N. and Zhai K. 2010 *Phys. Plasmas* **17** 056101
[17] Sugama H. and Nishimura S. 2002 *Phys. Plasmas* **9** 4637
[18] Pustovitov V.D. and Shafranov V.D. 1990 *Rev. Plasma Phys.* **15** 163
[19] Strand P.I. and Houlberg W.A. 2001 *Phys. Plasmas* **8** 2782